Tunable Acoustic Metasurface for Three-Dimensional Wave Manipulations

Wen Kang Cao,[1,2] Cheng Zhang,[3] Li Ting Wu,[1] Kai Qi Guo,[1] Jun Chen Ke,[1] Tie Jun Cui,[1,*] and Qiang Cheng[1,†]

[1] *State Key Laboratory of Millimeter Waves, Department of Radio Engineering, Southeast University, Nanjing 210096, China*

[2] *School of Mechanical Engineering, Guizhou University, Guiyang 550025, China*

[3] *Hubei Engineering Research Center of RF-Microwave Technology and Application, School of Science, Wuhan University of Technology, Wuhan 430070, China*

(Received 2 November 2020; revised 19 January 2021; accepted 25 January 2021; published 11 February 2021)

Acoustic metasurfaces display unprecedented potential for their unique and flexible capabilities of wave front manipulations. Although rapid progress and significant developments have been achieved in this field, it still remains a significant challenge to obtain an acoustic metasurface that can perform different functions in three-dimensional (3D) space, as desired. Here, a tunable acoustic metasurface composed of Helmholtz-resonator-like digital-coding meta-atoms is presented to overcome the limitation and realize 3D dynamic wave manipulations. The digital meta-atom is constructed from two cylindrical cavities controlled by a motor. By changing the depth of the bottom cavity with the motor automatically, the reflection phase of the meta-atom can be adjusted continuously over the range of nearly 360°, realizing the required digital states. To build the relationship between the digital-coding profiles and scattering patterns, convolution and addition operations are implemented. Based on such operations, various fascinating functionalities, such as arbitrary scattering-pattern shift and superposition of different scattering beams, are achieved. This study paves the way for studying acoustic metasurfaces from the digital perspective and provides efficient methods for realizing spatial acoustic wave control.

DOI: 10.1103/PhysRevApplied.15.024026

I. INTRODUCTION

Wave front modulation is of significant interest and has the powerful ability to control acoustic fields and electromagnetic fields. Recently, metasurfaces, as a classical two-dimensional (2D) metamaterial, comprising subwavelength artificial structures, have garnered significant attention and promoted substantial development, owing to their unique properties for controlling classic waves, including acoustic and electromagnetic (EM) waves [1–3]. In the acoustic region, metasurfaces provide great flexibility for controlling the phase and amplitude of reflected or transmitted waves; therefore, several intriguing functions, such as acoustic communication [4], acoustic asymmetric transmission [5,6], acoustic hologram [7,8], sound-diffuse reflection [9,10], and anomalous reflection or refraction [11–13], are implemented. In addition, inspired by EM-coding metasurfaces [14], acoustic coding metasurfaces are introduced for manipulations of the acoustic waves with high flexibility via mimicking the bits "0" and "1" in computer systems [15–17].

Although passive acoustic metasurfaces have achieved significant milestones in controlling acoustic waves [18, 19], their acoustic responses cannot always be altered because, once fabricated, the geometries of unit cells, such as membrane-type structures [20,21], Helmholtz resonators [22–24], and space-coiling structures [25–27], are fixed, hindering them from some special application scenarios that require tunable scattering patterns. Therefore, tunable acoustic metasurfaces are highly desired, and several researchers have focused on the design of tunable and reconfigurable acoustic metasurfaces or metamaterials [28–31]. Recently, programmable acoustic structures have been proposed to demonstrate acoustic topological insulators [32] and acoustic metasurfaces [33], achieving 2D wave manipulations. Additionally, tunable helical structures were utilized to flexibly control the reflection and transmission patterns in three-dimensional (3D) space [34,35], while the manual adjustment method seriously restricts their applications. Therefore, it is still difficult to achieve continuous and arbitrary control of scattering patterns by utilizing the existing acoustic metastructures.

Here, we propose a tunable acoustic metasurface, which comprises a Helmholtz-resonator-like digital-coding structure. Compared with passive meta-atoms [36–38], the wave-propagation paths inside the unit cell can be flexibly

*tjcui@seu.edu.cn
†qiangcheng@seu.edu.cn

tuned via a motor and the corresponding control system that can change the depth of the bottom cavity inside it; subsequently, the reflection phases of typical particles can be modulated continuously. To achieve flexible and diverse control of scattering beams using the proposed tunable acoustic metasurface, convolution and addition operations that are proposed to manipulate the scattering patterns of EM waves [39,40] are all introduced and implemented in this study. The consistency between the measured and simulated results verifies the validity of the corresponding theory.

II. DESIGN PRINCIPLE OF THE TUNABLE ACOUSTIC METASURFACE

A tunable acoustic metasurface constructed from an array with 8×8 programmable supercell elements (to mimic the local periodic boundary conditions, a supercell containing 3×3 identical unit cells is employed and controlled by a single motor) is provided for dynamic airborne sound control (Fig. 1). The basic unit cell comprises two cylindrical cavities with different depths (h_1 and h_2) and diameters (R_1 and R_2) [Fig. 2(a)], of which $h_1 = 4$ mm, $R_1 = 22$ mm, and $R_2 = 20$ mm are fixed. The period of the unit cell (p) is equal to 25 mm, which is approximately one third of the wavelength of the operating frequency (4600 Hz). In our design, each programmable element can be continuously modulated to obtain the required reflection phase with the help of a motor and the corresponding control system in Fig. 1, which can change the location of the movable plunger [Fig. 2(b)]. To reveal the relationship between the reflection phases and total depth

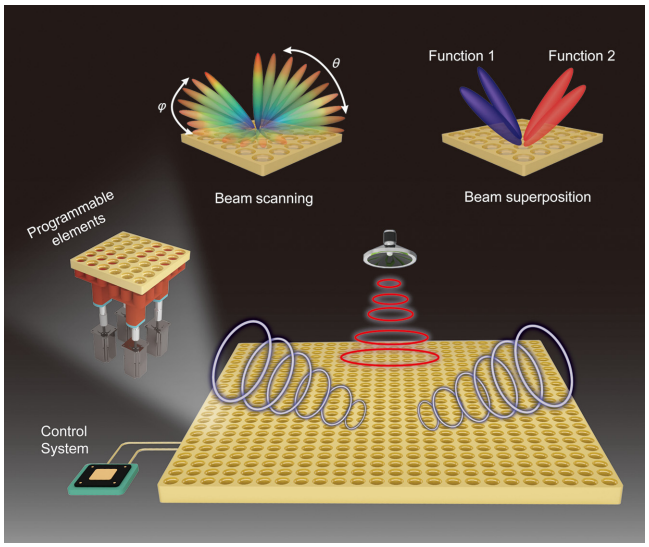

FIG. 1. Schematic of the proposed tunable acoustic metasurface that can carry out beam scanning and superposition, as shown at the top of this figure. Inset: Schematic of the basic programmable element.

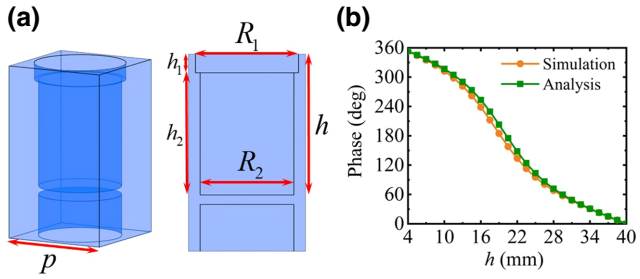

FIG. 2. (a) Unit cell of the tunable acoustic metasurface. Inset: Cross-section view of the unit cell. (b) Simulated and analytically calculated reflection phases of the typical unit cell as a function of total depths h.

$h(h = h_1 + h_2)$ of the cavities, the reflection phases of the unit cell [Fig. 2(b)] are calculated using the transfer-matrix method. From the calculated results, it is easy to observe that a nearly full 360° span of the reflection phase shift can be obtained at 4600 Hz, as h increases from 4 to 40 mm (see Appendix A for the detailed calculation process). Furthermore, the simulated results are provided here to verify the calculated results, and the small discrepancy between them has no significant effect on the design of the proposed acoustic metasurfaces. Here, the materials of the unit cells can be considered as acoustically rigid, whereas the thermoviscous losses are negligible. The simulation method and material parameters are presented in Appendix B. Additionally, to demonstrate the operational bandwidth of the proposed acoustic metasurface, the reflection phase spectrum of the unit cell between 4000 and 6000 Hz is presented in Appendix C, where h is varied from 5 to 31.9 mm. Due to the good linearity of the reflection phase curves, we can see that the phase differences are retained well in a broadband bandwidth among meta-atoms with different sizes, implying that the proposed metasurface can operate efficiently over the observed frequency range. Therefore, by properly arranging the aperture phase patterns across the proposed acoustic metasurface, the predesigned features can be realized, including arbitrary beam scanning and beam superposition.

Furthermore, it is clear that we can find cavities with different depths with almost full 360° control of the reflection phases. For example, when values of h are chosen to be 5 and 19 mm, the achieved phases are 0° and 180°, respectively, from Fig. 2(b). Therefore, the proposed structure can serve as the 0 or 1 units required by the coding metasurfaces [39,40]. By optimizing the coding sequences of the coding digits, the scattering pattern of the metasurface can be efficiently engineered, hereby fostering a number of applications, like beam splitting or beam deflection. In addition, since the plunger is able to move in real time, all unit cells can switch between different states, making the metasurface a tunable surface as a result. This means that different functionalities can be defined and adjusted by synthesizing the coding sequences in advance.

Next, to illustrate the excellent performance of far-field scattering-pattern regulations based on this tunable metasurface, mathematical operations, including convolution and addition, are revealed in Sec. III and Sec. IV to achieve single or multiple beam control on the basis of the proposed acoustic metasurface.

III. CONVOLUTION OPERATION ON THE ACOUSTIC METASURFACE

Steering of acoustic waves exhibits great applications in nondestructive evaluation [41] and acoustic imaging [42]. Although acoustic metasurfaces are demonstrated to shift acoustic waves to different directions, they still have limitations in fast and efficient 3D wave manipulations, which is an essential function for practical applications. Recently, the convolution operation proposed by Liu *et al.* was demonstrated to realize the continuous control of EM waves in arbitrary directions [39]. However, successful demonstrations in acoustic regions are scarce. Therefore, the convolution operation can be a useful method to regularize the far-field scattering patterns flexibly and arbitrarily from a fully digital perspective.

Because the acoustic pressure field distribution on the acoustic metasurface and the scattering pattern in the far-field region are a Fourier transform pair, the aperture field distribution, $P(x_\lambda)$, and the far-field scattering pattern, $P(\sin\theta)$, are related as per the following Fourier transform:

$$P(x_\lambda)\cdot e^{j\,2\pi x_\lambda \sin(\theta_0)} \overset{\text{FFT}}{\Leftrightarrow} P(\sin\theta)\times\delta(\sin\theta-\sin\theta_0) = P(\sin\theta-\sin\theta_0), \quad (1)$$

where $e^{j\,2\pi x_\lambda \sin(\theta_0)}$ describes the acoustic pressure field distribution with unity amplitude and gradient phase along a certain direction, $x_\lambda = x/\lambda$ denotes the equivalent physical length of the period of coding sequences relative to the operation wavelength λ, and θ denotes the deflection angle with respect to the normal direction. From Eq. (1), it is clear that the scattering pattern $P(\sin\theta)$ can deviate away from the original direction by $\sin\theta_0$ in the angular coordinate by multiplying the acoustic pressure field distribution $P(x_\lambda)$ and gradient phase sequence $e^{j\,2\pi x_\lambda \sin(\theta_0)}$ together. Here, the multiplication of the phases of two coding sequences is equivalent to the modulus of the corresponding coding digits, providing less computational complexity for the optimization of scattering patterns.

A 2-bit acoustic coding metasurface, which contains four types of coding elements to form a gradient coding sequence "0 1 2 3 0 1 2 3...," is proposed to verify the above concept of the scattering beam shift. The four digits represent four types of supercell elements with a phase difference of 90°. As shown in Fig. 2(b), to obtain the required coding particles, four digital-coding unit cells with different h are selected. Additionally, the dimensions of 1-bit, 2-bit, and 3-bit coding elements are all listed in Table I.

TABLE I. Dimensions of different h for the corresponding 1, 2, and 3 bit coding digits.

h (mm)	5	11.9	15	17.1	19	21.2	24.8	31.9
1 bit	0				1			
2 bit	0		1		2		3	
3 bit	0	1	2	3	4	5	6	7

To demonstrate the performance of the convolution operation, an example is presented to illustrate the scattering pattern shift. A single scattering beam pointing in a predesigned direction in the upper-half space can be generated when the acoustic metasurface is encoded with different coding sequences (Fig. 3). As shown in Figs. 3(a) and 3(b), the acoustic metasurfaces encoded with two different coding sequences, S1 (0 1 2 3 0 1 2 3) and S2 (0 0 1 1 2 2 3 3), along the x direction are illustrated, and the corresponding anomalous reflections with deflection angles of 14.4° and 7.1° (with respect to the z axis in the x-o-z plane) can also be revealed, as $\theta = \arcsin(\lambda/L)$ (L is the period of the coding sequence). This can be confirmed by the simulated 3D far-field sound-pressure-level (SPL) scattering patterns [Figs. 3(a) and 3(b)] and the corresponding 2D results in the x-o-z plane [Fig. 3(e), orange line for case 1 and cyan line for case 2]. Thus, by adding the coding sequence S1 to S2, coding sequence S3 (0 1 3 0 2 3 1 2) can be obtained to produce a single beam with a different scattering angle, as illustrated in Fig. 3(c). Similarly, when coding sequence S1 adds coding sequence S4 (3 3 2 2 1 1 0 0), which is equal to the distribution of sequence S2, but along the reverse direction, another coding sequence, S5 (3 0 0 1 1 2 2 3), can be generated [Fig. 3(d)], which can be considered as S1 minus S2. By observing the scattering patterns of the coding sequences S3 and S5, which are termed as cases 3 and 4 in Figs. 3(c) and 3(d), it is clear that the original single beams can deviate from the normal axis to different directions without distortion. In addition, to further demonstrate the theoretical-calculated results based on the principle of the scattering pattern shift, the deflection angles of cases 3 and 4 can be calculated from

$$\theta = \sin^{-1}(\sin\theta_1 \pm \sin\theta_2), \quad (2)$$

where θ_1 and θ_2 denote the deflection angles of the two original coding sequences that are added or subtracted [39]. It is clear that the theoretical-calculated deflecting angles of cases 3 and 4 are 21.9° and 7.2°, respectively, which are approximately equal to the results of the numerical simulations in Fig. 3(f). Furthermore, the simulated scattered acoustic pressure field distributions of cases 1–4 in the x-o-z plane are presented in Figs. 3(g)–3(j), to demonstrate that the scattering beams can be steered to the predesigned directions. Meanwhile, a sample is fabricated

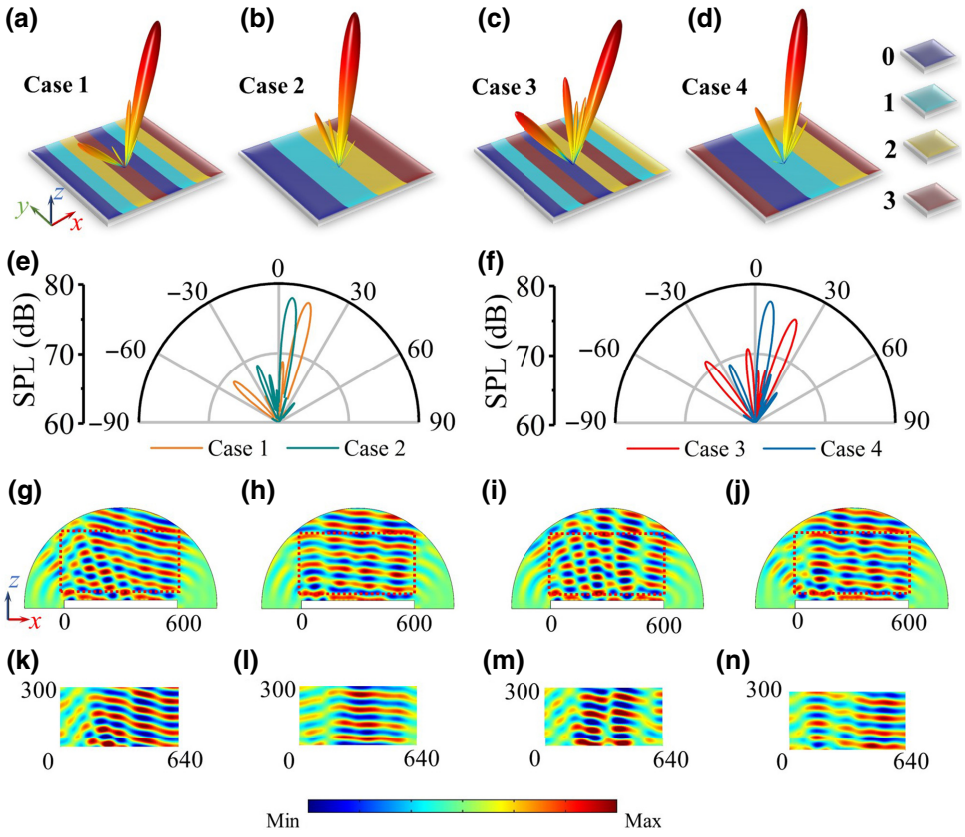

FIG. 3. Simulated and experimental results for a single scattering beam shift. (a)–(d) Coding patterns and corresponding 3D simulated scattering patterns for cases 1–4. (e),(f) Corresponding 2D simulated scattering patterns of cases 1–4 in the *x*-*o*-*z* plane. (g)–(j) Corresponding simulated scattered acoustic pressure field distributions and (k)–(n) measured results of cases 1–4 in the *x*-*o*-*z* plane. Measured areas are confined to the red dashed boxes.

and tested for comparison. Due to the instrument and site restrictions, only the near-field distributions can be measured in our home-built system. To generate the incident acoustic waves, a planer speaker (Panphonics SSHP 60×20) is used to generate a plane wave at 4600 Hz, which is driven by a power amplifier (Panphonics AA-160e) controlled by a dynamic signal acquisition module (NI USB-4431). A microphone with a diameter of 0.25 in. (BSWA MPA 416) is mounted on a motor with a step of 5 mm (approximately 1/15 wavelength at 4600 Hz) and used to measure sound within an area of 640×300 mm^2. Photographs of the sample and a detailed experimental setup can be found in Sec. V. The corresponding measured results for cases 1–4 are shown in Figs. 3(k)–3(n). No significant difference between the simulated and measured results can be discovered. Consequently, scattering beams with different deflection angles can be controlled easily in the elevation plane by performing a convolution operation on the proposed tunable acoustic metasurface.

In addition to the adjustment in the elevation plane, the convolution operation can also be used to realize the rotation of scattering patterns in the azimuthal direction. In particular, by adding two coding sequences with gradient phases along the x and y directions, the scattering beams can scan in a cutting plane with arbitrary azimuthal angles. Here, the elevation angle θ and azimuthal angle φ of the scattering beams can be calculated as follows [39]:

$$\theta = \sin^{-1}\left(\sqrt{\sin^2\theta_1 \pm \sin^2\theta_2}\right), \qquad \varphi = \tan^{-1}\left(\frac{\sin\theta_2}{\sin\theta_1}\right), \tag{3}$$

where θ_1 and θ_2 denote the elevation angles of the two original coding sequences with gradient phases along the x and y directions, respectively. To prove this principle, two cases are proposed in Appendix D to illustrate that scattering beams can be shifted to the predesigned elevation and/or azimuthal angles.

Consequently, scattering beams can be steered to the predesigned directions in the upper-half space, not only in the elevation direction, but also in the azimuthal direction by performing the convolution operation on the proposed tunable acoustic metasurface. The available deflecting angles of the acoustic metasurfaces are calculated as shown in Appendix E. According to the analysis in Appendix E, it is clear that the deflecting angles are no longer limited to a few values and can cover almost all areas in the upper-half space by performing the convolution operation of only four coding digits.

IV. ADDITION OPERATION ON THE ACOUSTIC METASURFACE

In Sec. III, with the aid of the convolution operation, scattering beams can be steered in the predesigned

direction. However, the realization of dynamic and independent control of multibeams within a single aperture is rather difficult in the acoustic region, whereas combining multiple functions into a single acoustic metasurface can significantly reduce the system complexity, making it convenient to realize system integration and miniaturization. Fortunately, the addition operation proposed by Wu *et al.* has been demonstrated to achieve the flexible superposition of several functions of EM metasurfaces [40]. However, the addition operation is not applied to the acoustic region. Therefore, it can be a meaningful method for designing multifunctional acoustic metasurfaces.

To illustrate the principle of the addition operation, complex coding digits are presented, which relate to the complex phase $e^{j\varphi}$ and involve entire phase information of acoustic waves. In particular, after the addition operation of two complex coding digits, a complex coding digit can be achieved and expressed as follows [40]:

$$Ae^{j\varphi_0} = e^{j\varphi_1} + e^{j\varphi_2}, \tag{4}$$

where A and φ_0 denote the magnitude and argument of the latter complex coding digit, respectively. φ_1 and φ_2 denote the arguments of the two original complex coding digits. Using the vector superposition principle, the information addition of two complex coding digits can be achieved. Therefore, through the addition of two or more coding patterns, the scattering patterns can be superposed together. It is important to indicate that, when the complex coding digits have reversed directions, the directions of the vector superposition results are anticlockwise. For instance, 1-bit complex coding digits additions $0_1 + 1_1 = 1_2$ and $1_1 + 0_1 = 3_2$ lead to different results. Notably, by adopting the addition operation, arbitrary-bit complex coding digits can be achieved with the 1-bit digits. A 3-bit coding metasurface is used in the following examples to exhibit these phenomena, of which eight different colors are used to represent eight coding digits (0 1 2 3 4 5 6 7) with a gradient phase of 45°.

To prove the above principle, we consider two complex 2-bit coding sequences, including sequence S1 (0 2 4 6 0 2 4 6) and sequence S4 (6 6 4 4 2 2 0 0). Single beams can be achieved with the proposed acoustic metasurface encoded with coding sequences S1 or S4, as shown in Figs. 3(a) and 3(b). After the addition operation of the above coding sequences along the x direction, a 3-bit coding sequence

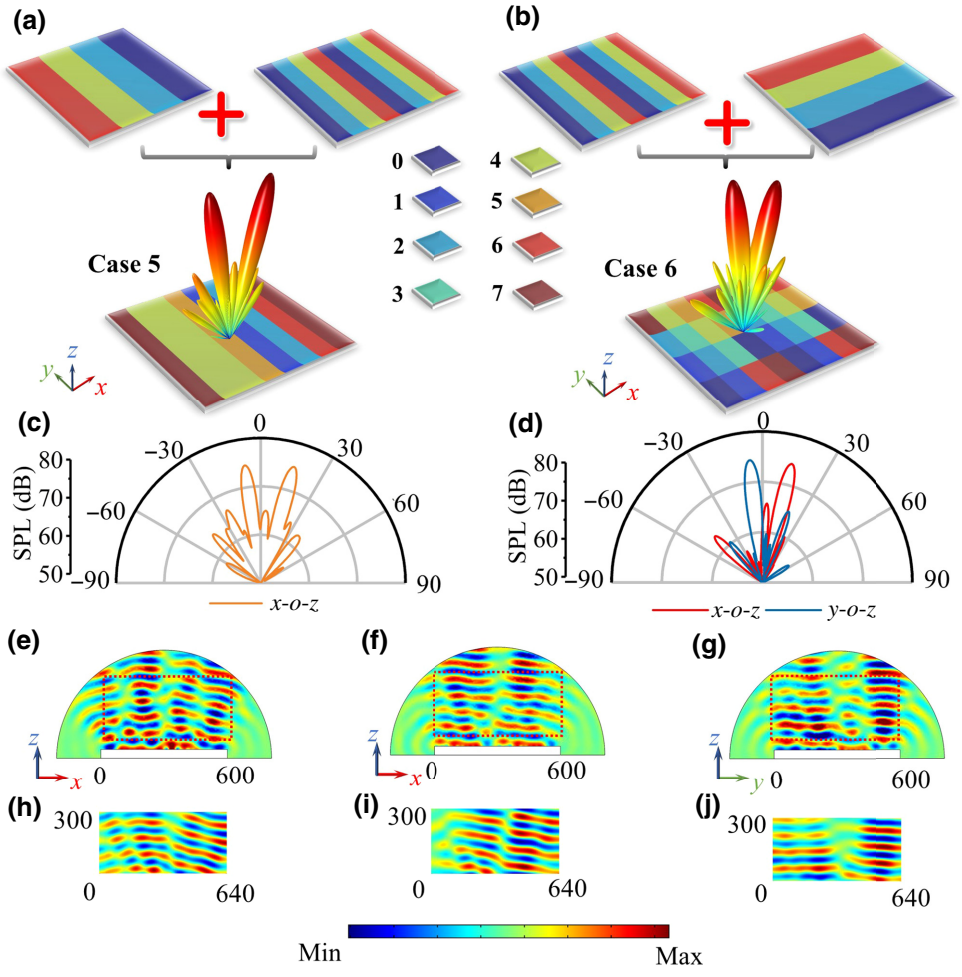

FIG. 4. Simulated and experimental results for the addition operation of two scattering beams. (a),(b) Coding patterns and simulated scattering patterns for cases 5 and 6. (c),(d) Simulated scattering patterns of case 5 in the x-o-z plane and case 6 in the x-o-z and y-o-z planes. (e)–(g) Simulated scattered acoustic pressure field distributions of (e) case 5 in the x-o-z plane and (f),(g) case 6 in the x-o-z and y-o-z planes. (h)–(j) Corresponding measured scattered acoustic pressure field distributions of cases 5 and 6. Measured areas are confined to the red dashed boxes.

can be obtained in Fig. 4(a), which is named as case 5. Notably, the subscripts on the coding digits are omitted in the coding sequences in Figs. 4(a) and 4(b). Meanwhile, the scattering patterns of case 5 are illustrated in Fig. 4(a), showing two scattering beams in the *x*-*o*-*z* plane, which are the superposed scattering beams of coding sequences S1 and S4. From the 2D scattering patterns (in the *x*-*o*-*z* plane) shown in Fig. 4(c), two scattering beams at $-7.7°$ and $14.8°$ are observed, which are approximately equal to the deflection angles of cases 1 and 2, respectively, in Fig. 3(e). The scattering pattern of case 5 verifies that scattering beams with different deflection angles can be superposed together with little interference through the proposed strategy. Finally, the scattering acoustic pressure field distributions of case 5 are also provided in Figs. 4(e) and 4(h), and the measured results correspond with the simulated results, further verifying this principle.

Similarly, scattering beams in different azimuthal directions can also be superposed by utilizing this method. In Fig. 4(b), a double-beam pattern can be achieved by adding the corresponding coding patterns. Figure 4(b) demonstrates the addition operation result (case 6) of the 2-bit coding sequences S1 (0 2 4 6 0 2 4 6, along the *x* direction) and S2 (0 0 2 2 4 4 6 6, along the *y* direction). The complex 3-bit coding sequence can achieve a complex scattering pattern, which is the superposition of the scattering patterns of coding sequences S1 and S2 along orthogonal directions [Fig. 4(b)], whereas the deflecting angles of the scattering beams with respect to the *z* axis are the same as those of cases 1 (in the *x*-*o*-*z* plane) and 2 (in the *y*-*o*-*z* plane). It is clear that the measured results [Figs. 4(i) and 4(j)] have excellent correspondence with the simulated results [Figs. 4(f) and 4(g)]. Through the above analysis, the scattering patterns of different coding sequences can be superposed along different directions via the addition operation, resulting in significant enhancement of the abilities of the proposed acoustic metasurfaces in regulating acoustic waves.

To illustrate the more powerful ability of the addition operation in generating more liberal scattering patterns, four scattering beams in the directions of $\varphi = 0°$, $90°$, $180°$, and $270°$ and three scattering beams in the directions of $\varphi = 0°$, $90°$, and $180°$ are further produced in Fig. 5. The former is the addition operation result of two identical 1-bit coding sequences S6 (0 4 0 4 0 4 0 4) along the *x* and *y* directions, respectively, whereas the

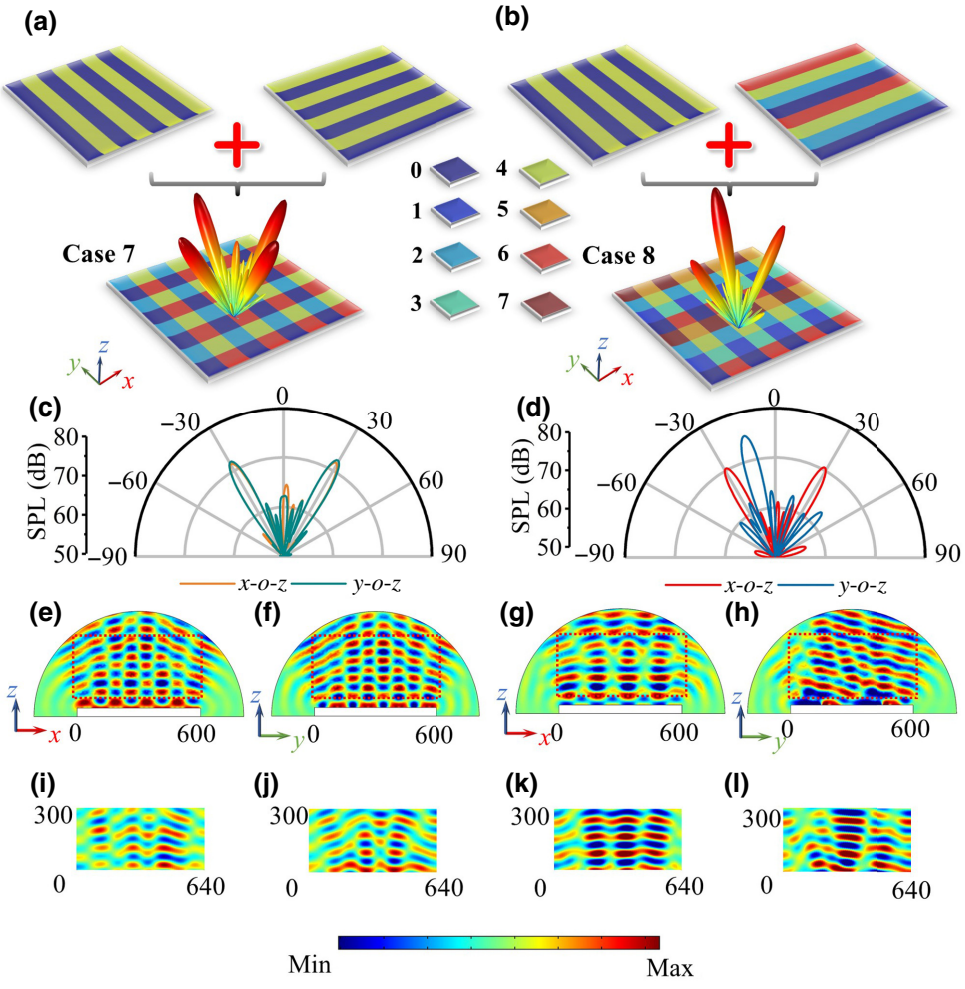

FIG. 5. Simulated and experimental results of four and three scattering beams by the addition operation. (a),(b) Coding patterns and corresponding simulated scattering patterns for cases 7 and 8. (c),(d) Simulated scattering patterns of cases 7 and 8 in the *x*-*o*-*z* and *y*-*o*-*z* planes. (e)–(h) Simulated scattered acoustic pressure field distributions of (e),(f) case 7 and (g),(h) case 8 in the *x*-*o*-*z* and *y*-*o*-*z* planes. (i)–(l) Corresponding measured scattered acoustic pressure field distributions of cases 7 and 8 in the *x*-*o*-*z* and *y*-*o*-*z* planes. Measured areas are confined to the red dashed boxes.

latter is generated by the addition operation of the 1-bit coding sequence S6 (0 4 0 4 0 4 0 4) and 2-bit coding sequence S1 (0 2 4 6 0 2 4 6) along the x and y directions, respectively. Here, two cases are referred to as case 7 and case 8. Because coding sequence S6 can generate two symmetrical scattering beams, after the addition operation, four scattering beams can be obtained in case 7 [Fig. 5(a)]. In Fig. 5(c), we can further observe that all deflecting angles of the four scattering beams (in the x-o-z planes and y-o-z planes) with respect to the z axis are 30°, which is nearly the same as that in theoretical calculations (29.8°). The simulated and measured scattered acoustic pressure field distributions in the x-o-z and y-o-z planes are shown in Figs. 5(e), 5(f), 5(i), and 5(j), and the results are highly consistent. We continue to explore the additive coding sequence of case 8. Two symmetrical scattering beams in the x-o-z plane and a single scattering beam in the y-o-z plane are shown in Fig. 5(b). Notably, the deflection angles of the obtained scattering beams [Fig. 5(d)] are approximately the same as those of the original coding sequences S6 and S1. Furthermore, the simulated scattered acoustic pressure field distributions of case 8 in the x-o-z and y-o-z planes [Figs. 5(g) and 5(h)] and the corresponding measured results [Figs. 5(k) and 5(l)] are also provided to prove the proposed principle, owing to the small difference.

Based on the proposed mathematical operations, the arbitrary shift and superposition of scattering beams can be achieved. To further expand the performance, we combine the convolution operation with the addition operation. Thus, multibeam scattering can be obtained and each scattering beam can be controlled independently; thus, the versatility of the proposed tunable acoustic metasurfaces is significantly expanded (see Appendix F).

V. EXPERIMENTAL VERIFICATION

To verify the feathers of the proposed tunable acoustic metasurface, a sample is fabricated that consists of 8×8 programmable elements. Figures 6(a) and 6(b) show photographs of the sample, including the tunable acoustic metasurface, the corresponding motor array, and the control system. The aluminum alloy and nylon are adopted to prepare the perforated plate and plungers, respectively. The experiment is conducted in a 3D open space. The acoustic pressure field distributions are recorded on a home-built near-field mapping system, and the experimental setup is shown in Fig. 6(c).

The total and incident acoustic fields are measured using the experimental setup with and without the acoustic metasurface. By subtracting the incident acoustic fields from total acoustic fields, scattered acoustic field distributions can be obtained, as shown in Figs. 3–5. The excellent correspondence between the simulation and measured results indicates that the proposed tunable acoustic metasurface

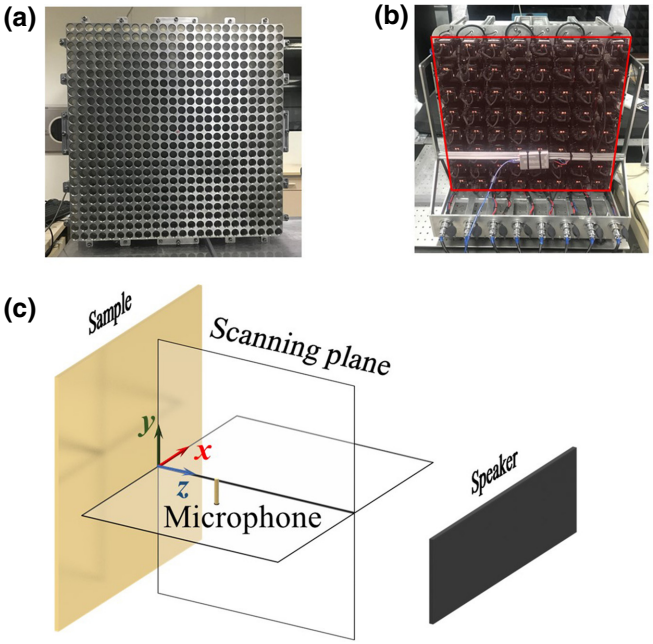

FIG. 6. (a) Photographs of the proposed tunable acoustic metasurface and (b) motor array with the corresponding control system. (c) Schematic of the experimental setup for measurements.

can achieve the designed functions. The small discrepancies between the simulated and measured results can be attributed to the displacement error of plungers and imperfect plane waves.

VI. CONCLUSION

We design, fabricate, and experimentally demonstrate a tunable acoustic metasurface that can flexibly achieve 3D wave manipulations by efficiently changing the inner structure of elements. By gradually modifying the cavity size of the basic element, with the help of a motor, the reflection phase can be tuned continuously. In addition, to obtain diverse scattering patterns, while flexibly controlling them, the convolution operation and addition operation are applied to acoustic regions. Based on the tunable acoustic metasurface, versatile wave-manipulation functions, including shifting the scattering beams to the predesigned direction and superimposing the scattering beams with different functions, are demonstrated numerically and experimentally. The measured results have excellent correspondence with the simulated results. Compared with previous tunable acoustic metasurfaces or metamaterials [33–35,43], the proposed acoustic metasurface can efficiently and continuously control the phase of reflected waves, thus achieving a variety of scattering patterns. In addition, if the operating speed of the motors can be sufficiently high and each unit cell can be independently controlled by external motors, the acoustic properties of

the proposed metasurface can be adjusted in time, and it can serve as a time-modulated system. As a result, it is reasonable to expect that the proposed tunable metasurface can be employed to implement intelligent devices with customized functionalities, such as acoustic information processing [44], acoustic communication [45], acoustic levitation [46,47], and acoustic space-time modulation [48,49].

ACKNOWLEDGMENTS

This work is supported by the National Key Research and Development Program of China under Grants No. 2017YFA0700201, No. 2017YFA0700202, No. 2018YFA0701904, and No. 2017YFA0700203; the National Natural Science Foundation of China (Grants No. 61731010 and No. 61722106); and the 111 Project (Grant No. 111-2-05).

W. K. Cao and C. Zhang contributed equally to this work.

APPENDIX A: ANALYTICAL DERIVATION OF THE REFLECTION PHASE φ OF THE UNIT CELL FOR NORMALLY INCIDENT WAVES

As shown in Fig. 7(a), the unit cell of the tunable acoustic metasurface can be divided into four regions (regions I, II, III, and IV) with different cross sections. The regions have different acoustic impedances. In Fig. 7(b), p_i and p_r represent the incident wave and reflected wave in region I, respectively. p_{it} and p_{ir} represent the transmitted and reflected waves in the ith region ($i = 2, 3, 4$). Here, region IV is considered to be infinitely long; thus, there are no reflected waves. Similar to the unit cell in Fig. 2(a), the widths of regions II and III are h_1 and h_2, respectively. The acoustic pressures and normal component of particle velocities in regions I to IV can be expressed as follows:

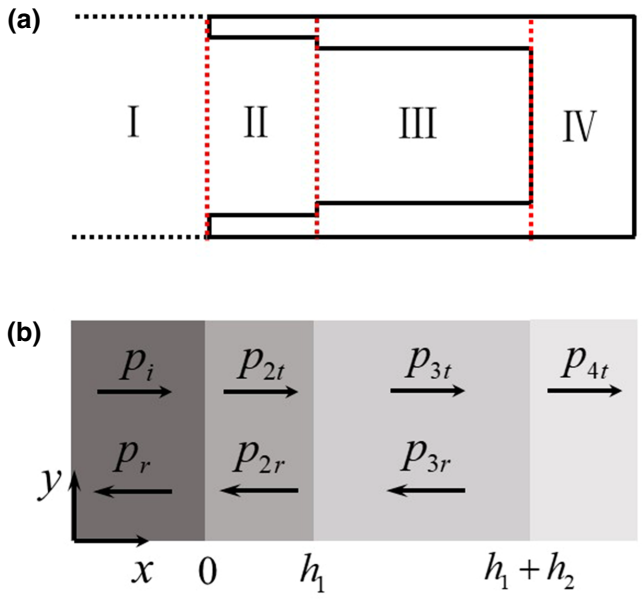

FIG. 7. Analytical model: (a) 2D schematic of the unit cell, which can be regarded as a four-layer structure with different acoustic impedances. (b) Analytical equivalence of the four-layer structure.

$$\begin{aligned} p_i &= p_{ia}e^{j(\omega t-kx)}, \quad p_r = p_{ra}e^{j(\omega t+kx)}, \\ v_i &= v_{ia}e^{j(\omega t-kx)}, \quad v_r = v_{ra}e^{j(\omega t+kx)}, \end{aligned} \tag{A1}$$

$$\begin{aligned} p_{2t} &= p_{2ta}e^{j(\omega t-kx)}, \quad p_{2r} = p_{2ra}e^{j(\omega t+kx)}, \\ v_{2t} &= v_{2ta}e^{j(\omega t-kx)}, \quad v_{2r} = v_{2ra}e^{j(\omega t+kx)}, \end{aligned} \tag{A2}$$

$$\begin{aligned} p_{3t} &= p_{3ta}e^{j[\omega t-k(x-h_1)]}, \quad p_{3r} = p_{3ra}e^{j[\omega t+k(x-h_1)]}, \\ v_{3t} &= v_{3ta}e^{j[\omega t-k(x-h_1)]}, \quad v_{3r} = v_{3ra}e^{j[\omega t+k(x-h_1)]}, \end{aligned} \tag{A3}$$

$$\begin{aligned} p_{4t} &= p_{4ta}e^{j[\omega t-k(x-h_1-h_2)]}, \\ v_{4t} &= v_{4ta}e^{j[\omega t-k(x-h_1-h_2)]}, \end{aligned} \tag{A4}$$

where p_{ia}, p_{ra}, p_{ita}, and p_{ira} and v_{ia}, v_{ra}, v_{ita}, and v_{ira} denote the amplitudes of the acoustic pressures and normal component of the particle velocities in the respective regions; ω is the angular frequency; and k is the wave number in air. Meanwhile, boundary conditions at the three interfaces between the four regions can be expressed as follows:

$$\begin{aligned} p_{ia} + p_{ra} &= p_{2ta} + p_{2ra}, \\ S_1(p_{ia} - p_{ra}) &= S_2(p_{2ta} - p_{2ra}), \end{aligned} \tag{A5}$$

$$\begin{aligned} p_{2ta}e^{-jkh_1} + p_{2ra}e^{jkh_1} &= p_{3ta} + p_{3ra}, \\ S_2(p_{2ta}e^{-jkh_1} - p_{2ra}e^{jkh_1}) &= S_3(p_{3ta} - p_{3ra}), \end{aligned} \tag{A6}$$

$$\begin{aligned} p_{3ta}e^{-jkh_2} + p_{3ra}e^{jkh_2} &= p_{4ta}, \\ \frac{p_{3ta}e^{-jkh_2} - p_{3ra}e^{jkh_2}}{Z_0} &= \frac{p_{4ta}}{Z_1}, \end{aligned} \tag{A7}$$

where, S_1, S_2 and S_3 denote the cross-section areas of regions I, II, and III, respectively. $Z_0 = \rho_0 c_0$ denotes the impedance of air (ρ_0 and c_0 are the density and speed of sound in air, respectively). Z_1 denotes the impedance of region IV. Because the materials of unit cells can be considered as acoustically rigid, Z_1 is much larger than Z_0.

Therefore, by employing Eqs. (A5)–(A7), we obtain the following relations of the acoustic pressure component between neighboring regions:

$$\begin{bmatrix} p_{2ta} \\ p_{2ra} \end{bmatrix} = M_1 \begin{bmatrix} p_{ia} \\ p_{ra} \end{bmatrix}, \tag{A8}$$

$$\begin{bmatrix} p_{3ta} \\ p_{3ra} \end{bmatrix} = M_2 \begin{bmatrix} p_{2ta} \\ p_{2ra} \end{bmatrix}, \tag{A9}$$

$$\begin{bmatrix} p_{4ta} \\ 0 \end{bmatrix} = M_3 \begin{bmatrix} p_{3ta} \\ p_{3ra} \end{bmatrix}, \tag{A10}$$

where

$$M_1 = \frac{1}{2}\begin{pmatrix} 1+S_{21} & 1-S_{21} \\ 1-S_{21} & 1+S_{21} \end{pmatrix}, \tag{A11}$$

$$M_2 = \frac{1}{2}\begin{bmatrix} (1+S_{32})e^{-jkh_1} & (1-S_{32})e^{jkh_1} \\ (1-S_{32})e^{-jkh_1} & (1+S_{32})e^{jkh_1} \end{bmatrix}, \tag{A12}$$

$$M_3 = \frac{1}{2}\begin{bmatrix} (1+Z_{01})e^{-jkh_2} & (1-Z_{01})e^{jkh_2} \\ (1-Z_{01})e^{-jkh_2} & (1+Z_{01})e^{jkh_2} \end{bmatrix}. \tag{A13}$$

Here, $S_{21} = (S_1/S_2)$, $S_{32} = (S_2/S_3)$, and $Z_{01} = (Z_1/Z_0) \gg 1$.

Finally, by using the transfer-matrix method, the overall matrix can be expressed in the following form:

$$M = M_3 M_2 M_1 = \begin{bmatrix} m_{11} & m_{12} \\ m_{21} & m_{22} \end{bmatrix}, \tag{A14}$$

where

$$\begin{aligned} m_{21} = {} & (1-Z_{01})(1+S_{32})(1+S_{21})e^{-jk(h_1+h_2)} \\ & + (1+Z_{01})(1-S_{32})(1+S_{21})e^{jk(h_2-h_1)} \\ & + (1-Z_{01})(1-S_{32})(1-S_{21})e^{jk(h_1-h_2)} \\ & + (1+Z_{01})(1+S_{32})(1-S_{21})e^{jk(h_1+h_2)}, \end{aligned} \tag{A15}$$

and

$$\begin{aligned} m_{22} = {} & (1-Z_{01})(1+S_{32})(1-S_{21})e^{-jk(h_1+h_2)} \\ & + (1+Z_{01})(1-S_{32})(1-S_{21})e^{jk(h_2-h_1)} \\ & + (1-Z_{01})(1-S_{32})(1+S_{21})e^{jk(h_1-h_2)} \\ & + (1+Z_{01})(1+S_{32})(1+S_{21})e^{jk(h_1+h_2)}. \end{aligned} \tag{A16}$$

The reflection coefficient, r, can be obtained from the elements in M as follows:

$$r = \frac{m_{21}}{m_{22}} = \frac{-(1+S_{32})[S_{21}\cos(kh) - j\,\sin(kh)] + (1-S_{32})[S_{21}\cos(kh') - j\,\sin(kh')]}{(1+S_{32})[S_{21}\cos(kh) + j\,\sin(kh)] - (1-S_{32})[S_{21}\cos(kh') + j\,\sin(kh')]}, \tag{A17}$$

where $h = h_1 + h_2$ and $h' = h_1 - h_2$.

Correspondingly, the phase, φ, of the reflection coefficient can be obtained as follows:

$$\varphi = \arg(r). \tag{A18}$$

The analytical result of the reflection phase φ calculated from Eq. (A18) is shown in Fig. 2(b). It is easy to see that the analysis results and the simulation results are almost identical.

APPENDIX B: SIMULATION METHOD AND MATERIAL PARAMETERS

The commercial software package COMSOL Multiphysics 5.2a, with the pressure acoustics module, is utilized to calculate the reflection phases of unit cells and near-field as well as far-field acoustic pressure distributions of the proposed tunable acoustic metasurface encoded with different coding sequences. The background medium is air, and the material of the unit cell is aluminum alloy, except for the movable plunger with nylon at the bottom. The material parameters of the unit cells and background media are listed in Table II. The walls of the unit cell can be viewed as acoustically rigid because the impedances of aluminum alloy and nylon are much larger than that of air. To obtain the reflection phase, a plane wave is incident along the $-z$ direction, and periodic boundary conditions are near the unit cell. Additionally, in the process of simulating the near-field and far-field acoustic pressure distributions, perfectly matched layers are added near the metasurface to reduce unnecessary reflections, and a plane wave is incident along the $-z$ direction with a 1 Pa amplitude.

TABLE II. Material parameters of unit cells and air.

Name	Density (kg/m^3)	Sound velocity (m/s)
Air	1.29	343
Aluminum alloy	2730	6340
Nylon	2600	1120

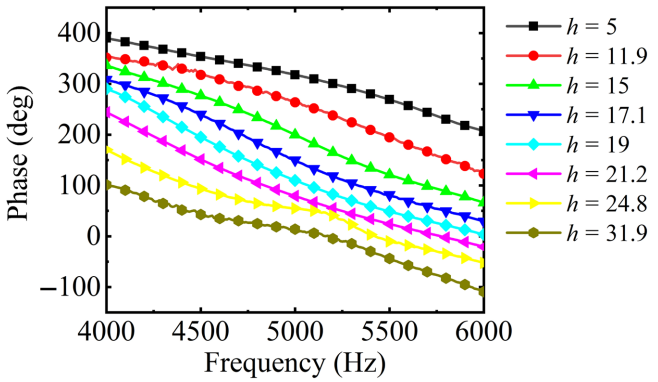

FIG. 8. Simulated reflection phase spectra of the unit cell between 4000 and 6000 Hz, when h is varied from 5 to 31.9 mm.

APPENDIX C: EFFECT OF THE OPERATIONAL FREQUENCY ON THE REFLECTION PHASES OF THE UNIT CELL

The reflection phases of the unit cell between 4000 and 6000 Hz are simulated in Fig. 8. It is clear that, as h increases from 5 to 31.9 mm, the phase differences remain approximately unchanged. Meanwhile, the geometry of the unit cells can be changed to maintain a reasonable reflection phase at other operational frequencies. From the results, we can conclude that the proposed metasurface can achieve similar functions to those in Figs. 3–5 within a broad operational bandwidth.

APPENDIX D: ROTATION OF SCATTERING BEAMS IN THE AZIMUTHAL DIRECTION

To prove that scattering beams can be rotated in the azimuthal direction, two cases are proposed to illustrate that a single scattering beam and double scattering beams can be rotated to the predesigned azimuthal angles. In particular, the first case shows that a single scattering beam can be rotated in the azimuthal direction when adding 2-bit coding sequences S2 (0 0 1 1 2 2 3 3) along the x direction and S1 (0 1 2 3 0 1 2 3) along the y direction [Fig. 9(a)]. Thereafter, the corresponding 3D scattering pattern can confirm the rotation of the scattering beam [Fig. 9(c)]. Meanwhile, for Eq. (3), the theoretical coordinates of the scattering beam are $\theta = 16.1°$ and $\varphi = 63.4°$ in the angular coordinate, which is consistent with the simulated results in Fig. 9(e). The second case shows that double scattering beams can be shifted by a certain angle in 3D space when adding the coding sequences S6 (0 2 0 2 0 2 0 2) with S1 (0 1 2 3 0 1 2 3) along the x and y directions, respectively [Fig. 9(b)]. According to the generalized Snell law, reflected waves of the metasurface encoded with coding sequence S6 propagate along two symmetrical directions in the x-o-z plane. Additionally, after adding coding sequences S6 and S1, the double scattering beams can be shifted to another direction.

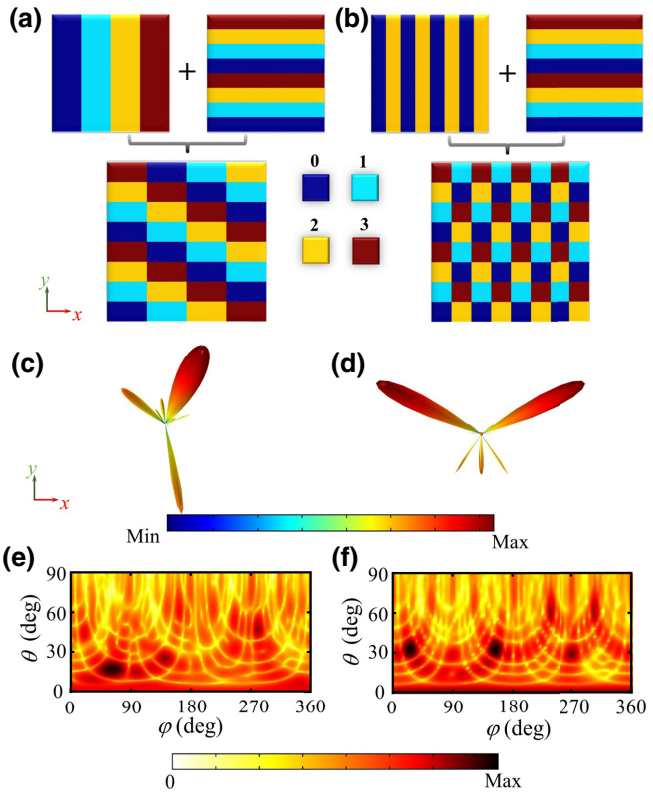

FIG. 9. Coding patterns and corresponding 3D and 2D scattering patterns to demonstrate the rotation of scattering beams in the azimuthal direction. (a) Schematic of rotating a single scattering beam with adding coding sequences S2 and S1 along x and y directions, respectively. (b) Schematic of rotating double scattering beams with adding coding sequences S6 and S1 along the x and y directions, respectively. (c),(d) Corresponding 3D scattering patterns and (e),(f) 2D scattering patterns of two cases.

The theoretical coordinates of the double scattering beams are $\theta = 33.8°$, $\varphi = 26.4°$ and$\theta = 33.8°$, $\varphi = 153.5°$. The simulated 3D and 2D scattering patterns in Figs. 9(d), and 9(f) confirm the theoretical results. Through the cases in Figs. 3 and 9, it is clear that scattering beams can scan in the entire upper-half space with high resolution, not only in the elevation direction, but also in the azimuthal direction.

APPENDIX E: QUANTITATIVE CALCULATIONS OF THE ATTAINABLE DEFLECTION ANGLES IN THE ELEVATION AND AZIMUTHAL PLANE

To verify the number of deflecting angles that can be achieved using the proposed unit cell in Fig. 2(a), based on Eq. (2), the attainable deflection angles θ of the scattering beams in the elevation plane are calculated from the modulus of two 2-bit coding sequences with gradient phases along the x direction first, as demonstrated in Fig. 10(a). Here, the horizontal and vertical axes represent the number of repetitions of coding digits of coding sequences "0 1 2 3 0 1 2 3. . . ." For example, coding sequences S1 (0 1 2

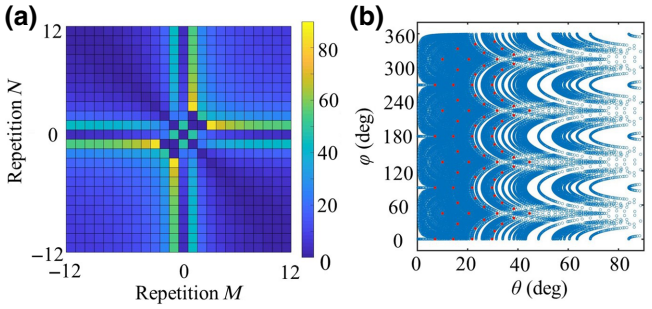

FIG. 10. Quantitative calculations of attainable deflecting angles in the elevation and azimuthal planes. (a) Calculated deflecting angles in the elevation plane obtained from the modulus of two 2-bit coding sequences along the x direction. Horizontal and vertical axes represent the number of repetitions M and N of the coding digits of two coding sequences, and minus sign indicates the coding sequence is reversed. (b) Calculated deflecting angles in the entire upper-half space obtained from the modulus of arbitrary two 2-bit coding sequences along the x and y directions. θ and φ are the elevation angle and the azimuthal angle of the scattering beams, respectively. Red dots represent deflecting angles that can be achieved by the proposed tunable acoustic metasurface.

3 0 1 2 3) and S2 (0 0 1 1 2 2 3 3) represent the situations of $M = 3$ and $N = 6$. The minus sign indicates that the coding sequence is reversed. As illustrated in Fig. 10(a), when the repetitions of coding digits increase from -12 to 12, the range of deflection angles is from 0° to 90°, except for some large angles, which is caused by a certain size of the period of unit cells. However, as multiple coding sequences with different repetition numbers are added along the same direction, the deflection angles can cover almost each angle from 0° to 90°.

To further demonstrate the deflecting-angle distributions of a single beam in the entire upper-half space, according to Eq. (3), two arbitrary 2-bit coding sequences in Fig. 10(a) are selected to add together along the x and y directions, respectively, to form a different sequence. The deflecting angles of the corresponding scattering beams can cover almost all areas in the upper-half space, as shown in Fig. 10(b). Notably, the red dots represent the deflection angles that can be achieved by the proposed tunable acoustic metasurface in Fig. 1 (M, $N = 0, \pm 3, \pm 6$).

APPENDIX F: MULTIBEAM SCATTERING IN ARBITRARY DIRECTIONS BY THE COMBINATION OF ADDITION AND CONVOLUTION OPERATIONS

When the addition operation of complex coding sequences is combined with the convolution operation, multibeam scattering in arbitrary directions can be obtained. Different from the rotation of the double scattering beams in Fig. 9 by the convolution operation, each

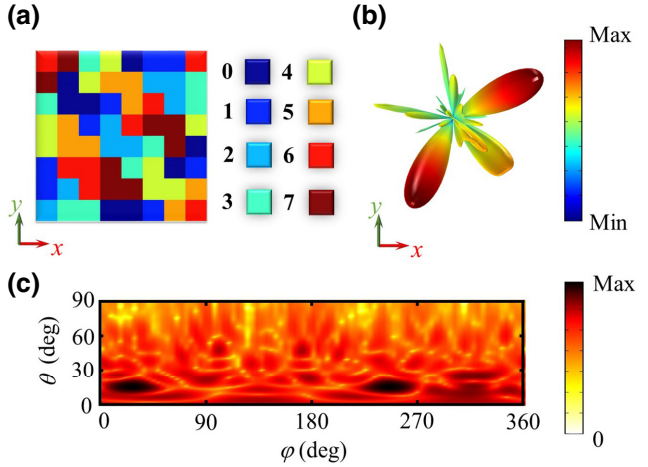

FIG. 11. Simulated results of multibeams scattering in arbitrary directions by the combination of the addition operation and the convolution operation. (a) Coding pattern. (b),(c) Corresponding 3D and 2D scattering patterns.

scattering beam can be controlled independently. First, two 2-bit coding sequences with different scattering patterns can be produced by the convolution operation, which are named as coding sequences C1 and C2. In particular, 2-bit coding sequence C1 is produced by the convolution operation of the 2-bit coding sequences S1 (0 2 4 6 0 2 4 6) and S2 (0 0 2 2 4 4 6 6) along the x and y directions, respectively. Similarly, another 2-bit coding sequence, C2, is produced by the convolution operation of 2-bit coding sequences S4 (6 6 4 4 2 2 0 0) along the x direction and S7 (6 4 2 0 6 4 2 0) along the y direction. Based on the principle of the convolution operation, coding sequences C1 and C2 can achieve a single scattering beam with different deflection angles in azimuthal directions. Consequently, after the addition of complex coding sequences C1 and C2, a 3-bit coding sequence is produced, as shown in Fig. 11(a). When two convoluted coding sequences are superposed together by the addition operation, it is clear that double scattering beams can be produced, where each scattering beam is controlled independently by the original 2-bit coding sequences C1 and C2 [Fig. 11(b)]. Based on Eq. (3), the coordinates of the scattering beams of the final 3-bit coding sequence in Fig. 11(b) are $\theta_1 = 16.1°$, $\varphi_1 = 26.7°$ and $\theta_2 = 16.1°$, $\varphi_2 = 243.4°$ in the angular coordinate. The results are shown by the 2D scattering pattern in Fig. 11(c).

[1] B. Assouar, B. Liang, Y. Wu, Y. Li, J.-C. Cheng, and Y. Jing, Acoustic metasurfaces, Nat. Rev. Mater. **3**, 460 (2018).

[2] H. Ge, M. Yang, C. Ma, M.-H. Lu, Y.-F. Chen, N. Fang, and P. Sheng, Breaking the barriers: Advances in acoustic functional materials, Natl. Sci. Rev. **5**, 159 (2018).

[3] A. M. Shaltout, V. M. Shalaev, and M. L. Brongersma, Spatiotemporal light control with active metasurfaces, Science **364**, 648 (2019).

[4] X. Jiang, B. Liang, J.-C. Cheng, and C.-W. Qiu, Twisted acoustics: Metasurface-enabled multiplexing and demultiplexing, Adv. Mater. **30**, 1800257 (2018).

[5] Y. Ge, H. X. Sun, S. Q. Yuan, and Y. Lai, Broadband unidirectional and omnidirectional bidirectional acoustic insulation through an open window structure with a metasurface of ultrathin hooklike meta-atoms, Appl. Phys. Lett. **112**, 243502 (2018).

[6] C. Shen, Y. Xie, J. Li, S. A. Cummer, and Y. Jing, Asymmetric acoustic transmission through near-zero-index and gradient-index metasurfaces, Appl. Phys. Lett. **108**, 223502 (2016).

[7] Y. Xie, C. Shen, W. Wang, J. Li, D. Suo, B.-I. Popa, Y. Jing, and S. A. Cummer, Acoustic holographic rendering with two-dimensional metamaterial-based passive phased array, Sci. Rep. **6**, 35437 (2016).

[8] Y. Zhu, J. Hu, X. Fan, J. Yang, B. Liang, X. Zhu, and J. Cheng, Fine manipulation of sound via lossy metamaterials with independent and arbitrary reflection amplitude and phase, Nat. Commun. **9**, 1632 (2018).

[9] Y. Zhu, X. Fan, B. Liang, J. Cheng, and Y. Jing, Ultrathin Acoustic Metasurface-Based Schroeder Diffuser, Phys. Rev. X **7**, 021034 (2017).

[10] W. K. Cao, L. T. Wu, C. Zhang, J. C. Ke, Q. Cheng, and T. J. Cui, A reflective acoustic meta-diffuser based on the coding meta-surface, J. Appl. Phys. **126**, 194503 (2019).

[11] A. Díaz-Rubio and S. A. Tretyakov, Acoustic metasurfaces for scattering-free anomalous reflection and refraction, Phys. Rev. B **96**, 125409 (2017).

[12] A. Díaz-Rubio, J. Li, C. Shen, S. A. Cummer, and S. A. Tretyakov, Power flow–conformal metamirrors for engineering wave reflections, Sci. Adv. **5**, eaau7288 (2019).

[13] L. Quan and A. Alù, Passive Acoustic Metasurface with Unitary Reflection Based on Nonlocality, Phys. Rev. Appl. **11**, 054077 (2019).

[14] T. J. Cui, M. Q. Qi, X. Wan, J. Zhao, and Q. Cheng, Coding metamaterials, digital metamaterials and programmable metamaterials, Light: Sci. Appl. **3**, e218 (2014).

[15] B. Xie, K. Tang, H. Cheng, Z. Liu, S. Chen, and J. Tian, Coding acoustic metasurfaces, Adv. Mater. **29**, 1603507 (2017).

[16] Y. Zhang, B. Xie, W. Liu, H. Cheng, S. Chen, and J. Tian, Anomalous reflection and vortex beam generation by multibit coding acoustic metasurfaces, Appl. Phys. Lett. **114**, 091905 (2019).

[17] B. Xie, H. Cheng, K. Tang, Z. Liu, S. Chen, and J. Tian, Multiband Asymmetric Transmission of Airborne Sound by Coded Metasurfaces, Phys. Rev. Appl. **7**, 024010 (2017).

[18] X. Wang, X. Fang, D. Mao, Y. Jing, and Y. Li, Extremely Asymmetrical Acoustic Metasurface Mirror at the Exceptional Point, Phys. Rev. Lett. **123**, 214302 (2019).

[19] B. Liang, J. C. Cheng, and C. W. Qiu, Wavefront manipulation by acoustic metasurfaces: From physics and applications, Nanophotonics **7**, 1191 (2018).

[20] J. Mei, G. Ma, M. Yang, Z. Yang, W. Wen, and P. Sheng, Dark acoustic metamaterials as super absorbers for low-frequency sound, Nat. Commun. **3**, 756 (2012).

[21] G. Ma, M. Yang, S. Xiao, Z. Yang, and P. Sheng, Acoustic metasurface with hybrid resonances, Nat. Mater. **13**, 873 (2014).

[22] Y. Li, C. Shen, Y. Xie, J. Li, W. Wang, S. A. Cummer, and Y. Jing, Tunable Asymmetric Transmission via Lossy Acoustic Metasurfaces, Phys. Rev. Lett. **119**, 035501 (2017).

[23] J. Li, C. Shen, A. Díaz-Rubio, S. A. Tretyakov, and S. A. Cummer, Systematic design and experimental demonstration of bianisotropic metasurfaces for scattering-free manipulation of acoustic wavefronts, Nat. Commun. **9**, 1342 (2018).

[24] X. Jiang, Y. Li, B. Liang, J. C. Cheng, and L. Zhang, Convert Acoustic Resonances to Orbital Angular Momentum, Phys. Rev. Lett. **117**, 034301 (2016).

[25] Y. Li, X. Jiang, R.-Q. Li, B. Liang, X.-Y. Zou, L.-L. Yin, and J.-C. Cheng, Experimental Realization of Full Control of Reflected Waves with Subwavelength Acoustic Metasurfaces, Phys. Rev. Appl. **2**, 064002 (2014).

[26] Y. Xie, W. Wang, H. Chen, A. Konneker, B.-I. Popa, and S. A. Cummer, Wavefront modulation and subwavelength diffractive acoustics with an acoustic metasurface, Nat. Commun. **5**, 5553 (2014).

[27] X. Zhu, K. Li, P. Zhang, J. Zhu, J. Zhang, C. Tian, and S. Liu, Implementation of dispersion-free slow acoustic wave propagation and phase engineering with helical-structured metamaterials, Nat. Commun. **7**, 11731 (2016).

[28] G. Ma, X. Fan, P. Sheng, and M. Fink, Shaping reverberating sound fields with an actively tunable metasurface, Proc. Natl. Acad. Sci. USA **115**, 6638 (2018).

[29] B.-I. Popa and S. A. Cummer, Non-reciprocal and highly nonlinear active acoustic metamaterials, Nat. Commun. **5**, 3398 (2014).

[30] B.-I. Popa, D. Shinde, A. Konneker, and S. A. Cummer, Active acoustic metamaterials reconfigurable in real time, Phys. Rev. B **91**, 220303(R) (2015).

[31] W. Ao, J. Ding, L. Fan, and S.-Y. Zhang, A robust actively-tunable perfect sound absorber, Appl. Phys. Lett. **115**, 193506 (2019).

[32] J.-P. Xia, D. Jia, H.-X. Sun, S.-Q. Yuan, Y. Ge, Q.-R. Si, and X.-J. Liu, Programmable coding acoustic topological insulator, Adv. Mater. **30**, 1805002 (2018).

[33] Z. Tian, C. Shen, J. Li, E. Reit, Y. Gu, H. Fu, S. A. Cummer, and T. J. Huang, Programmable acoustic metasurfaces, Adv. Funct. Mater. **29**, 1808489 (2019).

[34] S.-W. Fan, S.-D. Zhao, A.-L. Chen, Y.-F. Wang, B. Assouar, and Y.-S. Wang, Tunable Broadband Reflective Acoustic Metasurface, Phys. Rev. Appl. **11**, 044038 (2019).

[35] S.-D. Zhao, A. L. Chen, Y.-S. Wang, and C. Zhang, Continuously Tunable Acoustic Metasurface for Transmitted Wavefront Modulation, Phys. Rev. Appl. **10**, 054066 (2018).

[36] S. Qi and B. Assouar, Ultrathin acoustic metasurfaces for reflective wave focusing, J. Appl. Phys. **123**, 234501 (2018).

[37] Y. Zhu and B. Assouar, Multifunctional acoustic metasurface based on an array of Helmholtz resonators, Phys. Rev. B **99**, 174109 (2019).

[38] J. Li, W. Wang, Y. Xie, B.-I. Popa, and S. A. Cummer, A sound absorbing metasurface with coupled resonators, Appl. Phys. Lett. **109**, 091908 (2016).

[39] S. Liu, T. J. Cui, L. Zhang, Q. Xu, Q. Wang, X. Wan, J. Q. Gu, W. X. Tang, M. Q. Qi, J. G. Han, W. L. Zhang, X. Y. Zhou, and Q. Cheng, Convolution operations on coding metasurface to reach flexible and continuous controls of terahertz beams, Adv. Sci. **3**, 1600156 (2016).

[40] R. Y. Wu, C. B. Shi, S. Liu, W. Wu, and T. J. Cui, Addition theorem for digital coding metamaterials, Adv. Opt. Mater. **6**, 1701236 (2018).

[41] A. Leleux, P. Micheau, and M. Castaings, Long range detection of defects in composite plates using lamb waves generated and detected by ultrasonic phased array probes, J. Nondestr. Eval. **32**, 200 (2013).

[42] E. Mace, G. Montaldo, I. Cohen, M. Baulac, M. Fink, and M. Tanter, Functional ultrasound imaging of the brain, Nat. Methods **8**, 662 (2011).

[43] Y. Zhu, F. Fei, S. Fan, L. Cao, K. Donda, and B. Assouar, Reconfigurable Origami-Inspired Metamaterials for Controllable Sound Manipulation, Phys. Rev. Appl. **12**, 034029 (2019).

[44] F. Zangeneh-Nejad and R. Fleury, Performing mathematical operations using high-index acoustic metamaterials, New J. Phys. **20**, 073001 (2018).

[45] C. Shi, M. Dubois, Y. Wang, and X. Zhang, High-speed acoustic communication by multiplexing orbital angular momentum, Proc. Natl. Acad. Sci. USA **114**, 7250 (2017).

[46] A. Marzo, S. A. Seah, B. W. Drinkwater, D. R. Sahoo, B. Long, and S. Subramanian, Holographic acoustic elements for manipulation of levitated objects, Nat. Commun. **6**, 8661 (2015).

[47] A. Marzo and B. W. Drinkwater, Holographic acoustic tweezers, Proc. Natl. Acad. Sci. USA **116**, 84 (2019).

[48] J. Li, C. Shen, X. Zhu, Y. Xie, and S. A. Cummer, Nonreciprocal sound propagation in space-time modulated media, Phys. Rev. B **99**, 144311 (2019).

[49] C. Shen, X. Zhu, J. Li, and S. A. Cummer, Nonreciprocal acoustic transmission in space-time modulated coupled resonators, Phys. Rev. B **100**, 054302 (2019).